metals

Article

Effect of the Presence of Structural Defects on the Superconducting Properties of $(NbTa)_{0.67}(MoHfW)_{0.33}$ and Nb-47wt%Ti

Wojciech Nowak [1,2], Michał Babij [2], Aneta Hanc-Kuczkowska [3], Piotr Sobota [1,2], Adam Pikul [2] and Rafał Idczak [1,*]

1 Institute of Experimental Physics, University of Wrocław, pl. M. Borna 9, 50-204 Wrocław, Poland; wojciech.nowak@uwr.edu.pl (W.N.); piotr.sobota2@uwr.edu.pl (P.S.)
2 Institute of Low Temperature and Structure Research, Polish Academy of Sciences, ul. Okólna 2, 50-422 Wrocław, Poland; m.babij@intibs.pl (M.B.); a.pikul@intibs.pl (A.P.)
3 Institute of Materials Engineering, University of Silesia in Katowice, St. 75 Pułku Piechoty 1A, 41-500 Chorzów, Poland; aneta.hanc@us.edu.pl
* Correspondence: rafal.idczak@uwr.edu.pl

Abstract: A comparison of the results of studies on the influence of structural defects on the critical parameters of superconductivity has been made for the high-entropy alloy $(NbTa)_{0.67}(MoHfW)_{0.33}$ and for the conventional superconducting magnet material Nb-47wt%Ti. Positron annihilation lifetime spectroscopy (PALS), electrical resistivity, magnetization and magnetic susceptibility measurements were used. In addition, X-ray powder diffraction studies were performed on the high-entropy alloy $(NbTa)_{0.67}(MoHfW)_{0.33}$. Due to the rapid cooling of the materials after melting in the arc furnace, they contain a higher concentration of structural defects compared to the heat-treated materials. Magnetic property measurements showed that both the critical temperatures T_c and the upper critical fields $\mu_0 H_{c2}$ of bulk superconductivity-related materials are improved in the presence of structural defects.

Keywords: high-entropy alloy; superconductivity; X-ray powder diffraction; magnetic susceptibility measurements; positron annihilation lifetime spectroscopy

Citation: Nowak, W.; Babij, M.; Hanc-Kuczkowska A.; Sobota, P.; Pikul, A.; Idczak, R. Effect of the Presence of Structural Defects on the Superconducting Properties of $(NbTa)_{0.67}(MoHfW)_{0.33}$ and Nb-47wt%Ti. *Metals* **2023**, *13*, 1779. https://doi.org/10.3390/met13101779

Academic Editors: Michael R. Koblischka and Jiro Kitagawa

Received: 17 September 2023
Revised: 9 October 2023
Accepted: 18 October 2023
Published: 20 October 2023

1. Introduction

The presence of crystallographic defects (i.e., impurities, vacancies, and dislocations) can have significant effects on the superconducting properties of various metals and alloys [1]. For example, if the concentration of defects is sufficiently high, a material that is originally a type I superconductor becomes a type II superconductor. This effect has been convincingly demonstrated for tantalum [2,3] and rhenium [4]. Prozorov et al. have recently suggested that pure niobium is also a type I superconductor in the clean limit, but disorder (crystallographic defects, strain, stress) pushes it to become a type II superconductor [5]. Based on Reference [6], similar expectations can be made in the case of vanadium. All these observations can be explained by the assumption that crystallographic defects, or disturbances in composition [7,8], introduced into a pure crystal reduce the mean free path of electrons, leading to a shorter mean distance between electrons in the Cooper pairs. As a result, an increase in the penetration depth λ and a decrease in the coherence length ξ lead to an increase in the Ginzburg–Landau parameter $\kappa = \lambda/\xi$. The superconductor is classified as type I when κ is less than a critical value equal to $\kappa_c = 1/\sqrt{2} \approx 0.707$. If $\kappa > \kappa_c$, the superconductor is of type II. Another interesting aspect of the presence of the crystallographic defects in superconductors is related to the fact that the defects, acting as strong pinning centers, essentially influence the magnetic properties of the type II superconductor, i.e., by modifying the vortex structure, changing the reversible magnetization and/or increasing the critical current density J_c [9–12].

In view of the above, we decided to investigate the influence of crystallographic defects on the superconducting properties of the conventional Nb-47wt%Ti alloy as well as the recently discovered high-entropy alloy $(NbTa)_{0.67}(MoHfW)_{0.33}$ [13]. The presence of defects, mainly vacancies and dislocations, was studied using positron annihilation lifetime spectroscopy (PALS), a non-destructive and powerful experimental method for the detection and quantification of atomic-scale defects in various types of solids [14–16]. The superconducting properties of both alloys were determined by electrical resistivity and magnetic property measurements. The combination of PALS and DC magnetization data obtained for as-cast and annealed samples provides useful information about changes in the superconducting properties in the studied materials caused by the presence of crystallographic defects.

2. Materials and Methods

The $(NbTa)_{0.67}(MoHfW)_{0.33}$ and Nb-47wt%Ti samples were prepared from high-purity metals in the form of slugs and chips. The purity of used metals was as follows: 99.95% for Ta, 99.9% for Nb, 99.95% for Mo, 99.6% for Hf, 99.9% for W, and 99.99% for Ti. The synthesis was carried out by a conventional arc melting technique under a Ti-gettered purified argon atmosphere. In the case of the $(NbTa)_{0.67}(MoHfW)_{0.33}$ samples, all substrates were wrapped in tantalum foil prior to melting to prevent evaporation of elements with lower melting points. Both specimens were remelted several times to ensure alloy homogeneity and cooled rapidly to room temperature. These samples are referred to as the as-cast samples. In the next step, the specimens ingots were annealed in a vacuum furnace at 1170 K for 2 h (for the Nb-47wt%Ti sample) and at 1270 K for 2 h (for the $(NbTa)_{0.67}(MoHfW)_{0.33}$ sample). The samples were heated to the desired temperature and held for a certain time, then slowly cooled to room temperature. These specimens are referred to as the annealed samples.

The samples were subjected to crystal structure studies using powder X-ray diffraction measurements. A PANalytical X'pert Pro diffractometer with CuK_α radiation was used for this purpose. The aim of these studies was to confirm the phase purity of the material, both before and after annealing. The resulting patterns were analyzed by the Rietveld method using FullProf software [17].

Positron annihilation lifetime spectroscopy at room temperature was used to measure the content of crystallographic defects in the studied materials. The positron source was $^{22}NaCl$ evaporated on a thin Hostaphan foil. The obtained PALS spectra contained at least $1.5 \cdot 10^6$ counts. The spectra were then analyzed using the LT-9.0 program of Kansy [18], taking into account the correction for positron annihilation in the source setting.

The electrical resistivity of the studied materials was measured with a Quantum Design Physical Properties Measurement System platform using the four-point technique. A current density of 5 mA/cm with a frequency of 37 Hz was used in our experiment.

The magnetic properties of the materials were measured using a Quantum Design MPMS XL superconducting quantum interference device magnetometer. These measurements were performed in the temperature range of 1.8–15.0 K and in applied magnetic fields $\mu_0 H$ up to 9 T. The background from the sample holder (clean magnetic straw) with a magnetic moment $-4 \cdot 10^{-7}$ Am^2 at 1 T was subtracted form the raw data. All magnetic measurements were performed after zero-field cooling of the samples to 2.0 K.

3. Results and Discussion

3.1. Crystal Structure

The powder X-ray patterns shown in Figure 1 were obtained for $(NbTa)_{0.67}(MoHfW)_{0.33}$ and Nb-47wt%Ti specimens. Rietveld analysis confirmed that both alloys obtained from the arc furnace melting crystallized in a cubic, body-centered crystal structure (space group $Im\overline{3}m$) without secondary phases. In the case of $(NbTa)_{0.67}(MoHfW)_{0.33}$, the additional peak located at the position $2\theta \approx 26^o$ was recognized as the most intense reflection of graphite (0002) derived from the sample holder. The absence of additional phases indicates the mixing of all the elements that formed both alloys. They were randomly distributed throughout the crystal structure. The XRD patterns for $(NbTa)_{0.67}(MoHfW)_{0.33}$ and Nb-47wt%Ti specimens after annealing show the same crystal structure of the alloys. This shows that under thermal treatment, no temperature segregation of the components occurred.

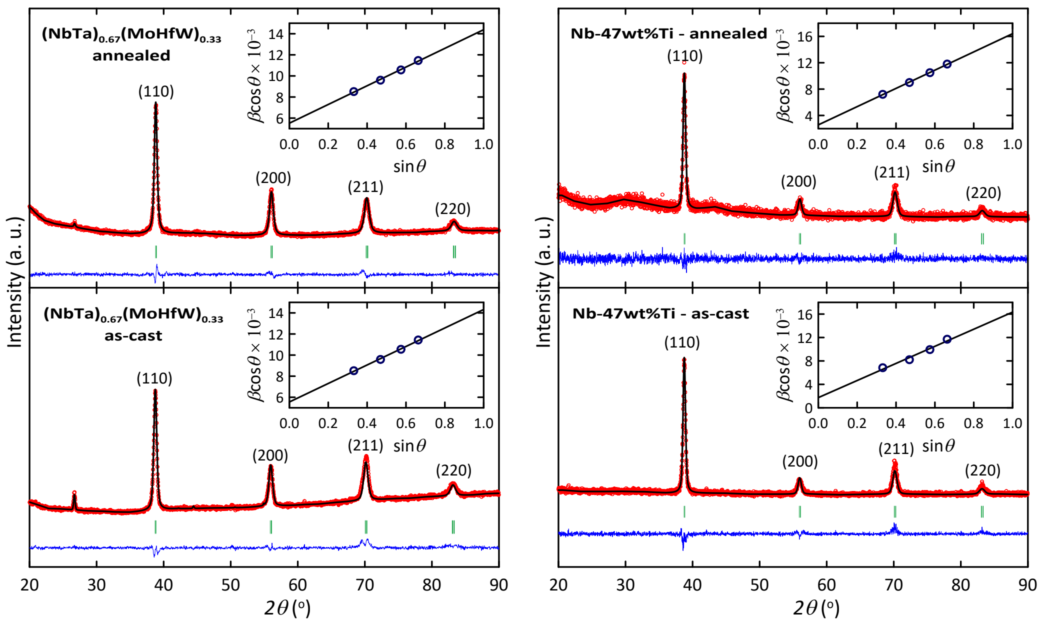

Figure 1. Powder X-ray diffraction patterns for annealed (**top**) and as-cast (**bottom**) samples of $(NbTa)_{0.67}(MoHfW)_{0.33}$ (**left**) and Nb-47wt%Ti (**right**) with the results of Ritveld refinement. Red circles are the experimental data, black lines are fitted theoretical curves, blue lines are the differences between the two, and green dashes show positions of the Bragg reflections described by the corresponding Miller indices. The insets show the Williamson–Hall plots, where solid lines are linear fits to experimental points.

For $(NbTa)_{0.67}(MoHfW)_{0.33}$, the Rietveld analysis showed that the lattice parameter for the as-cast sample is equal to $a = 3.286(1)$ Å, while for the annealed sample, it is slightly smaller and equal 3.281(1) Å. The results obtained are comparable with the lattice parameters of other high-entropy alloys with similar compositions, presented in the papers [19–22]. Considering the crystal lattice parameter of the components used in the bcc structure, Nb (3.301 Å), Ta (3.303 Å), Mo (3.147 Å), Hf (3.615 Å), and W (3.165 Å), the composition-averaged theoretical value of the lattice parameter $a_{th} = 3.304$ Å derived from Vegard's law [23] is slightly higher than the obtained values, which is reasonable due to the predominant content of Nb and Ta.

In the case of Nb-47wt%Ti, Rietveld analysis yields $a = 3.286(1)$ Å for the as-cast sample and $a = 3.285(1)$ Å for the annealed one, and these parameters are in good agreement with $a = 3.327$ Å determined for the bcc niobium–titanium alloy [24].

The Williamson–Hall method was used to determine the average grain size L and average internal stresses ϵ of the studied samples. Using the data obtained through Rietveld refinements of the obtained XRD patterns, a linear fit was determined and described by the formula [25]:

$$\beta\cos(\theta) = \epsilon\sin(\theta) + \frac{K\lambda}{L}, \tag{1}$$

where β is the full width at half maximum (FWHM) intensity in 2θ units, θ is the Bragg angle, λ is the X-ray wavelength, and $K = 0.9$ is the shape factor. This method showed that for the two $(NbTa)_{0.67}(MoHfW)_{0.33}$ samples, both grain size and strain do not change within the limits of experimental uncertainty and are equal to $L = 25(1)$ nm and $\epsilon \approx 0.89(4)\%$. In the case of Nb-47wt%Ti, the values of L and ϵ decreased slightly with annealing from $L = 80(39)$ nm and $\epsilon = 1.46(16)\%$ to $L = 53(3)$ nm and $\epsilon = 1.38(3)\%$.

3.2. Vacancy Concentration

The PALS spectra for both annealed and as-cast samples of $(NbTa)_{0.67}(MoHfW)_{0.33}$ and Nb-47wt%Ti are shown in Figure 2. Similar to our previous studies [3,4], all PALS spectra are described by three exponential components, characterized by the mean positron lifetimes τ, τ_{s1}, τ_{s2} and their intensities I, I_{s1}, I_{s2}. The component with the highest intensity $I \approx 90\%$ and the shortest mean lifetime τ is identified as the component resulting from the annihilation of electron–positron pairs in the bulk of the test material. On the other hand, the other components with intensities of $I_{s1} + I_{s2} \approx 10\%$ and much longer mean lifetimes $\tau_{s1} = 378$ ps and $\tau_{s2} = 1.78$ ns correspond to annihilation in the positron source and the Hostaphan foil.

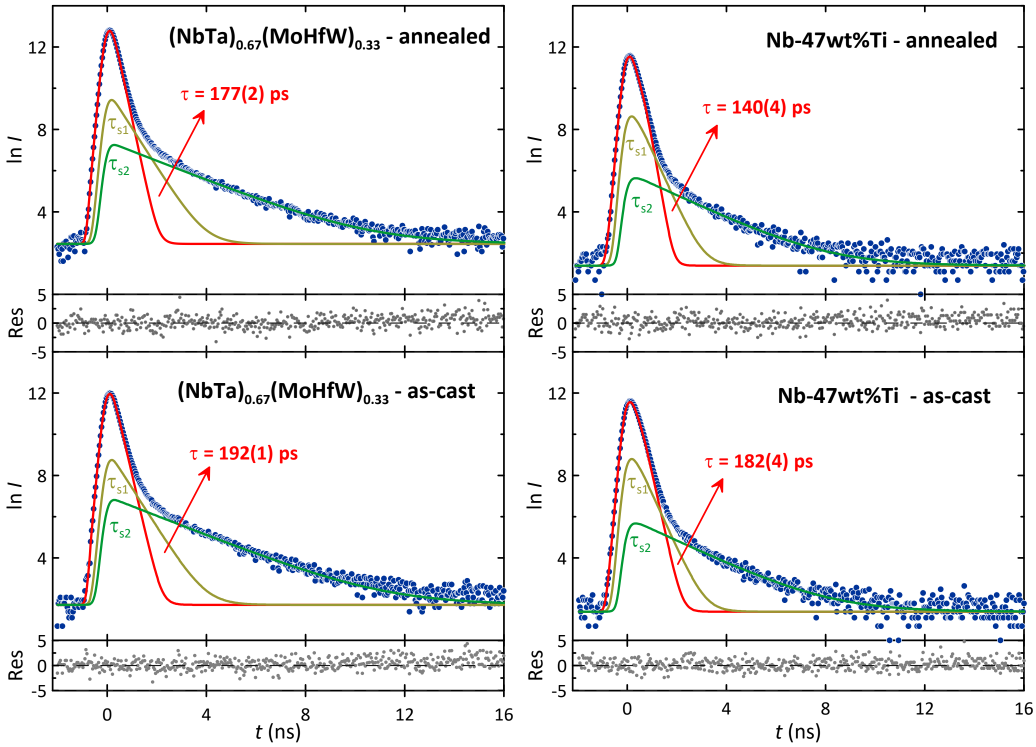

Figure 2. PALS spectra measured at room temperature for $(NbTa)_{0.67}(MoHfW)_{0.33}$ (**left**) and Nb-47wt%Ti (**right**), where the upper spectra represent measurements on annealed samples, while the lower spectra show measurements on as-cast samples, including fits of three exponent components. Red component is related to annihilation in the studied material, while the others correspond to annihilation in a positron source and in a Hostaphan foil.

For the Nb-47wt%Ti sample, PALS spectra showed a decrease in the average lifetime of positrons due to thermal treatment from $\tau = 182(4)$ ps for the as-cast sample to 140(4) ps for the annealed sample. According to the work [26], the positron bulk lifetimes τ_{bulk} for pure niobium and titanium are equal to 120 ps and 150 ps, respectively. At the same time, the positron monovacancy lifetimes τ_{vac} for those two metals are much longer and close to 210 ps and 222 ps, respectively. Taking these data into account, it could be stated that the annealed Nb-47wt%Ti sample with $\tau = 140(4)$ ps is almost free of any lattice defects, while $\tau = 182(4)$ ps obtained for the as-cast sample reveals the presence of numerous vacancies that were generated during the sample preparation procedure and frozen at room temperature.

The PALS spectra obtained for $(NbTa)_{0.67}(MoHfW)_{0.33}$ samples revealed a decrease in the number of structural defects due to annealing. The positron lifetimes decreased from 192(1) ps for the as-cast sample to 177(2) ps for the annealed sample. For pure metals, which are the components of this HEA, the positron bulk lifetimes τ_{bulk} are between 105 ps and 164 ps, while the positron monovacancy lifetimes τ_{vac} are in the range of 170 ps to

252 ps [26]. At the same time, Williamson–Hall plots taken from the XRD patterns presented in the previous section show that neither grain size nor strain changes significantly with heat treatment. Based on these facts, it can be postulated that the concentration of dislocations and grain boundaries does not change, while the content of point defects (mainly vacancies) decreases due to annealing. However, $\tau = 177(2)$ ps indicates that the number of vacancies in the annealed sample is still high. Such an effect may be caused by insufficient heating temperature and/or too short a heating time. A summary of the information obtained from XRD patterns and PALS spectra is given in Table 1.

Table 1. Highlights extracted from XRD patterns and PALS spectra for as-cast and annealed samples of $(NbTa)_{0.67}(MoHfW)_{0.33}$ and Nb-47wt%Ti, where a is the lattice parameter, L is the mean grain size, ϵ is the mean internal strain, R_{wp} is the weighted profile R-factor, R_{exp} is the expected R-factor, and τ is the mean positron lifetime.

Parameter	$(NbTa)_{0.67}(MoHfW)_{0.33}$		Nb-47wt%Ti	
	as-Cast	**Annealed**	**as-Cast**	**Annealed**
a (Å)	3.286(1)	3.281(1)	3.286(1)	3.285(1)
L (nm)	25(1)	25(1)	80(39)	53(3)
ϵ (%)	0.88(4)	0.89(4)	1.46(16)	1.38(3)
R_{wp} (%)	17.3	13.0	38.4	43.9
R_{exp} (%)	14.0	10.4	34.1	42.7
τ (ps)	192(1)	177(2)	182(4)	140(4)

3.3. Electrical Resistivity

Figure 3 shows the temperature dependence of the electrical resistivity measured for the $(NbTa)_{0.67}(MoHfW)_{0.33}$ sample before and after annealing in the range between 2 K and 300 K and in applied magnetic fields up to $\mu_0 H$ = 1.2 T. For both HEA samples, one can observe that the resistivity decreases with decreasing temperature, which reflects the metallic behavior. For the as-cast sample, the resistivity measured at temperatures above the transition to the superconducting state varies from 97 µΩ cm (at 5 K) to 132 µΩ cm (at 300 K), and the calculated value of residual resistivity ratio ($RRR = \rho_{300K}/\rho_{5K}$) is equal to 1.36. In the case of the annealed sample, the resistance decreased more than three times compared to the as-cast sample and varied between 27 µΩ cm (at 5 K) and 38 µΩ cm (at 300 K). The RRR parameter is 1.41. The observed decrease in electrical resistivity as well as the small increase in the RRR parameter is probably connected with the reduction in the number of structural defects in the bulk of the annealed HEA. It can be noted here that the rather small values of the RRR parameter are related to the polycrystalline nature of the studied samples as well as to the high degree of atomic disorder, which is a common feature of high-entropy alloys. Similar results were obtained for other HEA and presented in the papers [27–30].

At temperatures below 5 K, the sudden drops in resistivity which are presented in the insets in Figure 3 are associated with the transition of the sample to the superconducting state. In a zero magnetic field, the temperature at which the resistance reaches zero decreases from 4.5(1) K for the as-cast sample to 4.2(2) K for the annealed one. As one can expect, for both studied HEA samples, the transition temperatures systematically decrease with increases in the external magnetic field $\mu_0 H$.

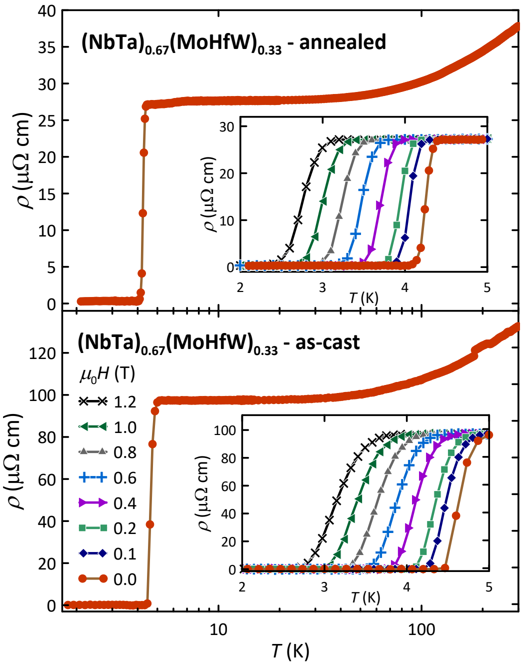

Figure 3. Electrical resistivity ρ of the as-cast and annealed samples of $(NbTa)_{0.67}(MoHfW)_{0.33}$ measured in a zero magnetic field as a function of temperature in the range from 2 K to 300 K. Insets show $\rho(T)$ dependencies measured in various applied fields $\mu_0 H$.

3.4. Magnetic Properties

3.4.1. $(NbTa)_{0.67}(MoHfW)_{0.33}$

The results of the magnetic property measurements are shown in Figure 4. Panel (a) shows the temperature dependence of the magnetic molar susceptibility χ for both (i.e., as-cast and annealed) samples of $(NbTa)_{0.67}(MoHfW)_{0.33}$. The measurements were performed in a zero-field cooling regime with a nominal field of 5 mT in the temperature range of 1.8–6 K. In addition, the figure shows the critical temperatures of the superconducting transition, which are 4.3(1) K for the as-cast sample and 4.0(1) K for the annealed sample. Panel (b) shows the dependence of the mass magnetization σ on the applied magnetic field $\mu_0 H$ for the annealed sample (top) and the as-cast sample (bottom). These measurements were made at temperatures of 2.0, 2.3, 2.6, 2.9, 3.2, 3.5, and 3.8 K. The insets show the dependence of $\sigma(\mu_0 H)$ for low applied fields. The magnetization data show that $(NbTa)_{0.67}(MoHfW)_{0.33}$ exhibits behavior characteristic of a type II superconductor, with a noticeably faster collapse of the vortex phase in the case of the annealed sample. This effect is more pronounced at higher temperatures. The transition of the material to the normal state (upper critical field) was derived from the point of intersection of the magnetization curve at a given temperature with $\sigma = 0$.

To the $\mu_0 H_{c2}(T)$ data collected in this way, we applied the Werthamer–Helfand–Hohenberg (WHH) model for BCS superconductors in the dirty limit, with the spin-paramagnetic effect (described by the Maki parameter α_M) and the spin–orbit scattering constant λ_{SO} [31–33]:

$$\ln\frac{1}{t} = \left(\frac{1}{2} + \frac{i\lambda_{SO}}{4\gamma}\right)\psi\left(\frac{1}{2} + \frac{\overline{h} + \frac{1}{2}\lambda_{SO} + i\gamma}{2t}\right) + \left(\frac{1}{2} - \frac{i\lambda_{SO}}{4\gamma}\right)\psi\left(\frac{1}{2} + \frac{\overline{h} + \frac{1}{2}\lambda_{SO} - i\gamma}{2t}\right) - \psi\left(\frac{1}{2}\right), \quad (2)$$

where $t = \frac{T}{T_c}$, $\gamma \equiv \sqrt{(\alpha_M \overline{h})^2 - (\frac{1}{2}\lambda_{SO})^2}$, $\overline{h} = \frac{4}{\pi^2}\frac{H_{c2}}{-dH_{c2}(T)/dT}$, and ψ is a digamma function. The solid lines in Figure 5 are the theoretical curves simulated with Equation (2), which we found to be the best fit to the experimental data. For both the as-cast and the annealed samples, the spin–orbit scattering constant was found to be negligible, so it was set to 0. In the case of the other parameters (i.e., the critical temperature and the Maki parameter), we found a significant change: from $\alpha_M = 0.30$, $T_c = 3.9(2)$ K for the as-cast sample to $\alpha_M = 0.23$, $T_c = 3.6(2)$ K for the annealed sample. The observed reductions result in a decrease in $\mu_0 H_{c2}(0)$ from 1.5(1) T to 1.1(1) T before and after sample annealing, respectively. For comparison, the theoretical curves calculated assuming the absence of the spin-paramagnetic effect and the spin–orbit scattering ($\alpha_M = 0.0$ and $\lambda_{SO} = 0.0$ [32]) are shown as dashed lines.

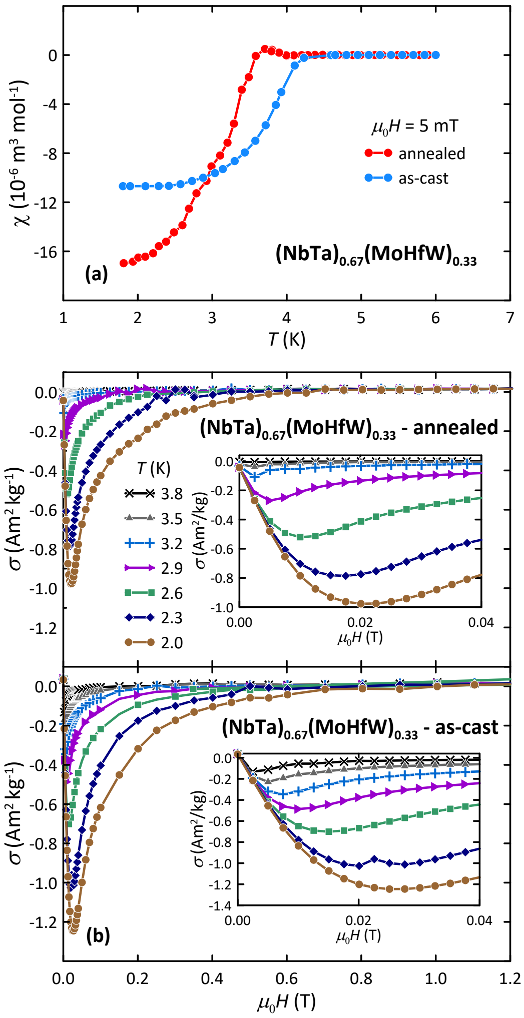

Figure 4. (**a**) Molar magnetic susceptibility χ of as-cast and annealed samples of $(NbTa)_{0.67}(MoHfW)_{0.33}$ measured as a function of temperature in a nominal applied magnetic field $\mu_0 H = 5$ mT in s zero-field cooling (ZFC) regime. (**b**) Dependence of mass magnetization σ on applied magnetic field $\mu_0 H$ measured at several temperatures on annealed (**top**) and as-cast (**bottom**) $(NbTa)_{0.67}(MoHfW)_{0.33}$ samples; the insets display $\sigma(\mu_0 H)$ in low fields. Lines have been added to guide the eye.

The estimated Maki parameter reveals important insights into the mechanism of Cooper pair breakup in a magnetic field. According to [33], α_M can be expressed by the equation:

$$\alpha_M = \sqrt{2}\frac{H_{c2}^{orb}}{H_P}, \tag{3}$$

where H_{c2}^{orb} is the orbital-limited upper critical field and H_P is the Pauli limiting field, which is given by the relation [34]:

$$\mu_0 H_P = 1.84 T_c. \tag{4}$$

Taking the determined values of T_c, one can obtain $\mu_0 H_P = 7.2(4)$ T for the as-cast sample and $\mu_0 H_P = 6.6(4)$ T for the annealed one. Knowing the values of α_M and H_P, it is possible to calculate H_{c2}^{orb} using Equation (3). The values of $\mu_0 H_{c2}^{orb} = 1.53(8)$ T and

$\mu_0 H_{c2}^{orb} = 1.07(7)$ T obtained, respectively, for the as-cast and annealed samples indicate that the superconductivity in studied material is orbital-limited.

In the next step, the Ginzburg–Landau coherence length ξ_{GL} and the Ginzburg–Landau penetration depth λ_{GL} can be estimated using the following equations [35,36]:

$$\xi_{GL} = \sqrt{\frac{\phi_0}{2\pi\mu_0 H_{c2}(0)}} \quad (5)$$

and

$$\lambda_{GL} = 6.42 \times 10^{-3}\sqrt{\frac{\rho_{\Omega cm}}{T_c}}, \quad (6)$$

where ϕ_0 is the magnetic flux quantum and $\rho_{\Omega cm}$ stands for the low-temperature normal-state resistivity in Ωcm units. It was found that $\xi_{GL} = 14.8(1)$ nm and $\lambda_{GL} = 320(4)$ nm in the case of the as-cast sample, while for the annealed one, $\xi_{GL} = 17.3(1)$ nm and $\lambda_{GL} = 176(3)$ nm. This finding confirms that the presence of crystallographic defects in the as-cast HEA sample leads to a shorter mean distance between electrons in the Cooper pairs, which results in an increase in the penetration depth λ_{GL} and a decrease in the coherence length ξ_{GL}. Finally, as expected, the Ginzburg–Landau parameter $\kappa = 21.6(3)$ calculated for the as-cast sample is much higher than for the annealed one, for which $\kappa = 10.2(2)$. However, both these values are higher than the critical value of $1/\sqrt{2}$, indicating that $(NbTa)_{0.67}(MoHfW)_{0.33}$ is a type II superconductor.

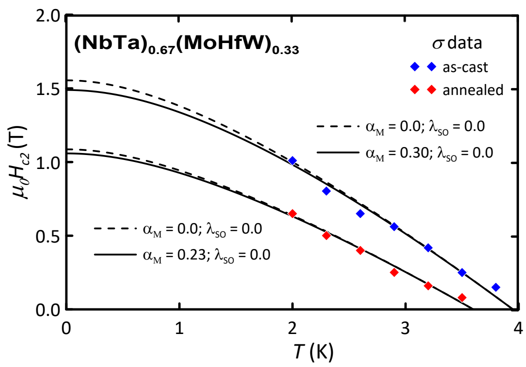

Figure 5. Upper critical field of $(NbTa)_{0.67}(MoHfW)_{0.33}$ as a function of temperature, derived from the magnetization data. Solid and dashed lines are simulations of the WHH curve (Equation (2)) to the experimental points, as described in the text.

3.4.2. Nb-47wt%Ti

The results of the bulk magnetization and magnetic susceptibility measurements are shown in Figure 6. The shape of the $\sigma(\mu_0 H)$ curves (Figure 6a) confirms that both the as-cast and the annealed materials are type II superconductors, but in the case of the annealed sample, the magnetic signal was found to be much weaker, which is consistent with the $\chi(T)$ data shown in Figure 6b. As in the case of $(NbTa)_{0.67}(MoHfW)_{0.33}$, the magnetic property data were used to construct the phase diagram $\mu_0 H_{c2}(T)$ for both the as-cast and annealed samples. The WHH model was then applied as described above, and the results of simulating the WHH curves (Equation (2)) for selected parameter sets are shown as solid and dashed lines in Figure 7. Such a procedure revealed that the Maki parameter and the spin–orbit scattering constant for this material do not change after annealing and are equal to $\alpha_M = 1.8$, $\lambda_{SO} = 0.8$ for both samples. The only parameter that changed was the critical temperature, which dropped from 9.2(1) K to 8.9(1) K after the material was heat treated, determining the change in the resulting upper critical field at 0 K from 15.1(3) T for the as-cast sample to 14.6(3) T for the annealed sample.

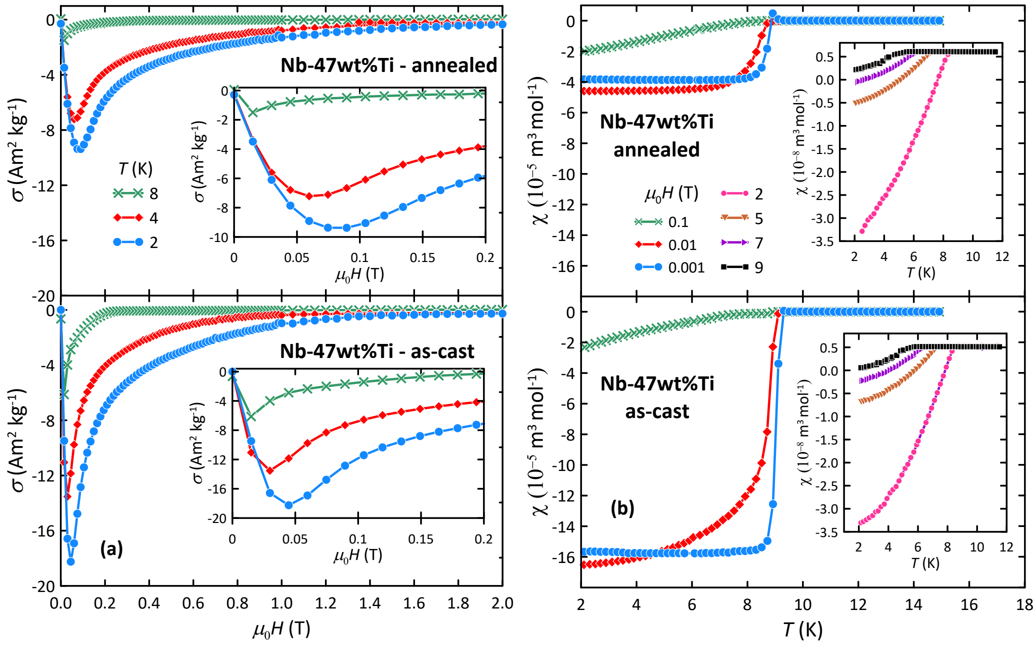

Figure 6. Low-temperature magnetic properties of Nb-47wt%Ti: (**a**) DC mass magnetization σ as a function of the applied field $\mu_0 H$ measured at various temperatures, (**b**) temperature dependence of the molar magnetic susceptibility χ in various applied fields.

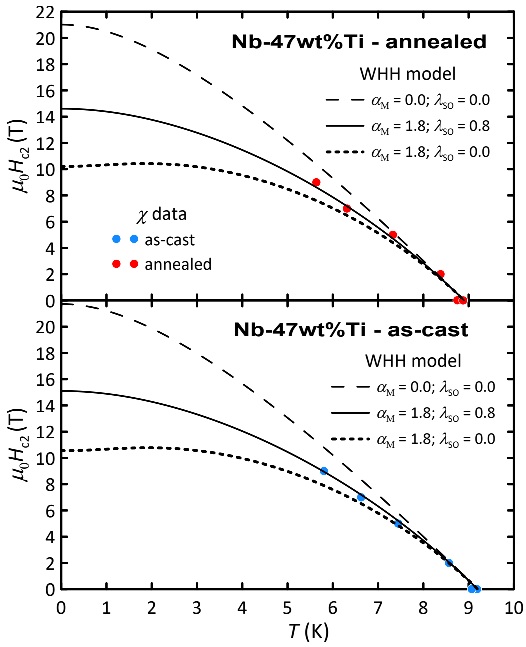

Figure 7. Upper critical filed of Nb-47wt%Ti as a function of temperature and derived magnetic property data. Solid and dashed lines are simulated WHH curves (Equation (2)), as described for $(NbTa)_{0.67}(MoHfW)_{0.33}$ (see text).

For comparison, Figure 7 also shows two additional theoretical curves derived from the WHH model (Equation (2)) for each sample. The first one (dashed lines) was derived by assuming the absence of both the spin paramagnetism and the spin–orbit effect, while the second one (dotted curves) was obtained by assuming the existence of only the Pauli spin paramagnetism described by the Maki parameter of 1.8.

As was shown, in the case of Nb-47wt%Ti, the thermal treatment does not affect the value of the Maki parameter. The H_{c2}^{orb} and H_P fields determined using Equations (3) and (4) are equal to $\mu_0 H_{c2}^{orb} = 21.5(3)$ T and $\mu_0 H_P = 16.9(2)$ T for the as-cast sample and

$\mu_0 H_{c2}^{orb} = 20.9(3)$ T and $\mu_0 H_P = 16.4(2)$ T for the annealed alloy. These values clearly show the dominant Pauli-limited H_{c2} behavior in the studied Nb-47wt%Ti alloy. Moreover, the influence of the structural defects on the superconducting properties of the studied materials is rather small.

4. Conclusions

Table 2 shows a summary of the most important information for the materials studied. It includes the mean positron lifetimes, values of T_c and $\mu_0 H_{c2}(0)$ obtained using WHH model, and the other fundamental parameters of the superconducting state.

Table 2. Summary of the most important information about the studied materials, where τ is the mean lifetime of positrons, T_c is the critical temperature, α_M is the Maki parameter, λ_{SO} is the spin–orbit scattering constant, $\mu_0 H_{c2}(0)$ is the upper critical field at 0 K, $\mu_0 H_P$ is the Pauli limiting field, $\mu_0 H_{c2}^{orb}$ is the orbital-limited upper critical field, ξ_{GL} is the Ginzburg–Landau coherence length, λ_{GL} is the Ginzburg–Landau penetration depth, and κ is the Ginzburg–Landau parameter.

$(NbTa)_{0.67}(MoHfW)_{0.33}$	as-Cast	Annealed	Nb-47wt%Ti	as-Cast	Annealed
τ (ps)	192(1)	177(2)	τ (ps)	182(4)	140(4)
T_c (K)	3.9(2)	3.6(2)	T_c (K)	9.2(1)	8.9(1)
α_M	0.30	0.23	α_M	1.8	1.8
λ_{SO}	0.0	0.0	λ_{SO}	0.8	0.8
$\mu_0 H_{c2}(0)$ (T)	1.5(1)	1.1(1)	$\mu_0 H_{c2}(0)$ (T)	15.3(3)	14.6(3)
$\mu_0 H_P$ (T)	7.2(4)	6.6(4)	$\mu_0 H_P$ (T)	16.9(2)	16.4(2)
$\mu_0 H_{c2}^{orb}$ (T)	1.53(8)	1.07(7)	$\mu_0 H_{c2}^{orb}$ (T)	21.5(3)	20.9(3)
ξ_{GL} (nm)	14.8(1)	17.3(1)			
λ_{GL} (nm)	320(4)	176(3)			
κ	21.6(3)	10.2(2)			

Our PALS experiments performed on polycrystalline samples of $(NbTa)_{0.67}(MoHfW)_{0.33}$ and Nb-47wt%Ti have shown that in both systems, the average lifetime of positrons decreases significantly after heat treatment of the samples, indicating a decrease in the concentration of point defects in their volume, as expected. This reduction has been found to be associated with a deterioration in the main superconductivity parameters of these two alloys (see Table 2), i.e., the critical temperature and the upper critical field.

Analysis of the experimental data obtained for $(NbTa)_{0.67}(MoHfW)_{0.33}$ using the WHH model has shown that the change in the upper critical field is accompanied by changes in both the critical temperature and the Maki parameter, the latter being identified with the Pauli paramagnetism effect and depending on the average transport scattering length [36]. In the case of the reference material Nb-47wt%Ti, on the other hand, the change in the upper critical field is mainly due to a change in the critical temperature, since the Maki parameter and the spin–orbit scattering constant remain unchanged.

Author Contributions: Conceptualization, R.I. and W.N.; validation, R.I. and A.P.; formal analysis, R.I., W.N., P.S. and A.P.; investigation, R.I., W.N., M.B., P.S. and A.H.-K.; resources, R.I., M.B. and A.P.; writing—original draft preparation, W.N., R.I. and A.P.; visualization, W.N.; project administration, R.I.; funding acquisition, R.I. All authors have read and agreed to the published version of the manuscript.

Funding: This research was funded by the National Science Center (Poland) under the OPUS 20 Project No. 2020/39/B/ST5/01782. For the purpose of Open Access, the author has applied a CC-BY public copyright license to any Author Accepted Manuscript (AAM) version arising from this submission.

Institutional Review Board Statement: Not applicable.

Informed Consent Statement: Not applicable.

Data Availability Statement: The data presented in this study are openly available in the OSF repository at DOI 10.17605/OSF.IO/G4N6B.

Conflicts of Interest: The authors declare no conflict of interest. The funders had no role in the design of the study; in the collection, analyses, or interpretation of data; in the writing of the manuscript; or in the decision to publish the results.

References

1. Mangin, P.; Kahn, R. *Superconductivity: An Introduction*; Springer International Publishing AG: Cham, Switzerland, 2017.
2. Sandu, V.; Cimpoiasu, E. Irreversibility in Rolled Tantalum. *J. Supercond. Nov. Magn.* **2018**, *31*, 2047–2054. [CrossRef]
3. Idczak, R.; Nowak, W.; Babij, M.; Tran, V. Type-II superconductivity in cold-rolled tantalum. *Phys. Lett. A* **2020**, *384*, 126750. [CrossRef]
4. Idczak, R.; Nowak, W.; Babij, M.; Tran, V. Influence of severe plastic deformation on superconducting properties of Re and In. *Phys. Supercond. Its Appl.* **2021**, *590*, 1353945. [CrossRef]
5. Prozorov, R.; Zarea, M.; Sauls, J.A. Niobium in the clean limit: An intrinsic type-I superconductor. *Phys. Rev. B* **2022**, *106*, L180505. [CrossRef]
6. Weber, H.; Moser, E.; Seidl, E.; Schmidt, F. Superconductivity and Hc2-anisotropy in vanadium. *Physica B+C* **1981**, *107*, 295–296. [CrossRef]
7. Khan, H. Microstructure related superconducting and mechanical properties of some Nb-Ti alloys with additions of Ta and Zr. *IEEE Trans. Magn.* **1983**, *19*, 745–748. [CrossRef]
8. Hariharan, Y.; Janawadkar, M.P.; Radhakrishnan, T.S.; Terrance, A.L.E.; Dixit, G.A.; Raghunathan, V.S. Structure property correlations in superconducting Ti-Nb alloys. *Pramana* **1986**, *26*, 513–524. [CrossRef]
9. Kiuchi, M.; Matsushita, T. Flux Pinning Characteristics in $YBa_2Cu_3O_7$ with Columnar Defects. In *Proceedings of the Advances in Superconductivity VIII*; Hayakawa, H., Enomoto, Y., Eds.; Springer: Tokyo, Japan, 1996; pp. 497–500.
10. Schönenberger, A.; Larkin, A.; Heeb, E.; Geshkenbein, V.; Blatter, G. Strong Pinning and Plastic Deformations of the Vortex Lattice. *Phys. Rev. Lett.* **1996**, *77*, 4636–4639. [CrossRef] [PubMed]
11. Braverman, G.M.; Gredeskul, S.A.; Avishai, Y. Mesoscopic superconducting disc with short-range columnar defects. *Phys. Rev. B* **1999**, *59*, 12039–12047. [CrossRef]
12. Zhou, W.; Xing, X.; Wu, W.; Zhao, H.; Shi, Z. Second magnetization peak effect, vortex dynamics and flux pinning in 112-type superconductor $Ca_{0.8}La_{0.2}Fe1-xCoxAs_2$. *Sci. Rep.* **2016**, *6*, 22278. [CrossRef]
13. Sobota, P.; Topolnicki, R.; Ossowski, T.; Pikula, T.; Pikul, A.; Idczak, R. Superconductivity in the high-entropy alloy $(NbTa)_{0.67}(MoHfW)_{0.33}$. *Phys. Rev. B* **2022**, *106*, 184512. [CrossRef]
14. Selim, F. Positron annihilation spectroscopy of defects in nuclear and irradiated materials—A review. *Mater. Charact.* **2021**, *174*, 110952. [CrossRef]
15. Jodi, D.E.; Listyawan, T.A.; Hruska, P.; Cizek, J.; Park, N.; Lee, U. Study of vacancies in $Fex(CoCrMnNi)_{100-x}$ medium- and high-entropy alloys by positron annihilation spectroscopy. *Scr. Mater.* **2021**, *194*, 113654. [CrossRef]
16. Lu, E.; Zhao, J.; Makkonen, I.; Mizohata, K.; Li, Z.; Hua, M.; Djurabekova, F.; Tuomisto, F. Enhancement of vacancy diffusion by C and N interstitials in the equiatomic FeMnNiCoCr high entropy alloy. *Acta Mater.* **2021**, *215*, 117093. [CrossRef]
17. Rodríguez-Carvajal, J. Recent advances in magnetic structure determination by neutron powder diffraction. *Phys. Condens. Matter* **1993**, *192*, 55–69. [CrossRef]
18. Kansy, J. Microcomputer program for analysis of positron annihilation lifetime spectra. *Nucl. Instruments Methods Phys. Res. Sect. A* **1996**, *374*, 235–244. [CrossRef]
19. Koželj, P.; Vrtnik, S.; Jelen, A.; Jazbec, S.; Jagličić, Z.; Maiti, S.; Feuerbacher, M.; Steurer, W.; Dolinšek, J. Discovery of a Superconducting High-Entropy Alloy. *Phys. Rev. Lett.* **2014**, *113*, 107001. [CrossRef]
20. von Rohr, F.O.; Cava, R.J. Isoelectronic substitutions and aluminium alloying in the Ta-Nb-Hf-Zr-Ti high-entropy alloy superconductor. *Phys. Rev. Mater.* **2018**, *2*, 034801. [CrossRef]
21. Vrtnik, S.; Koželj, P.; Meden, A.; Maiti, S.; Steurer, W.; Feuerbacher, M.; Dolinšek, J. Superconductivity in thermally annealed Ta-Nb-Hf-Zr-Ti high-entropy alloys. *J. Alloys Compd.* **2017**, *695*, 3530–3540. [CrossRef]
22. Kitagawa, J.; Hoshi, K.; Kawasaki, Y.; Koga, R.; Mizuguchi, Y.; Nishizaki, T. Superconductivity and hardness of the equiatomic high-entropy alloy HfMoNbTiZr. *J. Alloys Compd.* **2022**, *924*, 166473. [CrossRef]
23. Vegard, L. Die Konstitution der Mischkristalle und die Raumfüllung der Atome. *Z. FüR Phys.* **1921**, *5*, 17–26. [CrossRef]
24. Massalski, T.B. *Binary Alloy Phase Diagrams*, 2nd ed.; ASM: Materials Park, OH, USA, 1990.
25. Williamson, G.; Hall, W. X-ray line broadening from filed aluminium and wolfram. *Acta Metall.* **1953**, *1*, 22–31. [CrossRef]
26. Robles, J.M.C.; Ogando, E.; Plazaola, F. Positron lifetime calculation for the elements of the periodic table. *J. Phys. Condens. Matter* **2007**, *19*, 176222. [CrossRef] [PubMed]
27. Nelson, W.L.; Chemey, A.T.; Hertz, M.; Choi, E.; Graf, D.E.; Latturner, S.; Albrecht-Schmitt, T.E.; Wei, K.; Baumbach, R.E. Superconductivity in a uranium containing high entropy alloy. *Sci. Rep.* **2020**, *10*, 4717. [CrossRef] [PubMed]
28. Liu, B.; Wu, J.; Cui, Y.; Zhu, Q.; Xiao, G.; Wu, S.; Cao, G.; Ren, Z. Superconductivity in hexagonal Nb-Mo-Ru-Rh-Pd high-entropy alloys. *Scr. Mater.* **2020**, *182*, 109–113. [CrossRef]

29. Kitagawa, J.; Hamamoto, S.; Ishizu, N. Cutting Edge of High-Entropy Alloy Superconductors from the Perspective of Materials Research. *Metals* **2020**, *10*, 1078. [CrossRef]
30. Bogale, G.M.; Shiferaw, D.A. Iron-Based Superconductors. In *High Entropy Materials*; Zhang, Y., Ed.; IntechOpen: Rijeka, Croatia, 2022; Chapter 12. [CrossRef]
31. Helfand, E.; Werthamer, N.R. Temperature and Purity Dependence of the Superconducting Critical Field, H_{c2}. II. *Phys. Rev.* **1966**, *147*, 288–294. [CrossRef]
32. Werthamer, N.R.; Helfand, E.; Hohenberg, P.C. Temperature and Purity Dependence of the Superconducting Critical Field, H_{c2}. III. Electron Spin and Spin-Orbit Effects. *Phys. Rev.* **1966**, *147*, 295–302. [CrossRef]
33. Maki, K. Effect of Pauli Paramagnetism on Magnetic Properties of High-Field Superconductors. *Phys. Rev.* **1966**, *148*, 362–369. [CrossRef]
34. Clogston, A.M. Upper Limit for the Critical Field in Hard Superconductors. *Phys. Rev. Lett.* **1962**, *9*, 266–267. [CrossRef]
35. Tinkham, M. *Introduction to Superconductivity*; Dover Books on Physics Series; Dover Publications: Mineola, NY, USA, 2004.
36. Orlando, T.P.; McNiff, E.J.; Foner, S.; Beasley, M.R. Critical fields, Pauli paramagnetic limiting, and material parameters of Nb_3Sn and V_3Si. *Phys. Rev. B* **1979**, *19*, 4545–4561. [CrossRef]